Quasi-static and dynamic indentation of offshore pipelines with and without multi-layer polymeric coating

Ole Vestrum[a,b,*], Martin Kristoffersen[a,b], Mario A. Polanco-Loria[c], Håvar Ilstad[c], Magnus Langseth[a,b], Tore Børvik[a,b]

[a] *Structural Impact Laboratory (SIMLab), Department of Structural Engineering, Norwegian University of Science and Technology (NTNU), Trondheim, Norway*
[b] *Centre for Advanced Structural Analysis (CASA), NTNU, Trondheim, Norway*
[c] *Equinor Research Centre, Arkitekt Ebbells vei 10, Trondheim, Norway*

Abstract

Offshore pipelines are occasionally subjected to accidental impact loads from trawl gear or anchors, which may damage the pipe. In this study, a series of indentation experiments carried out on offshore steel pipes covered by a multi-layer polymeric coating solution is presented. Polymeric coating solutions are often applied to pipelines to act as corrosion protection and thermal insulation. Despite not being designed for it, the polymeric coatings are experienced to have an energy absorbing capacity, which is the main topic of the investigation herein. In design codes and guidelines, coatings are traditionally not accounted for when determining the energy absorbed by a pipeline during impact. This makes estimates overly conservative. The main goal of this experimental work is thus to investigate the contribution a typical polymeric coating makes to the energy absorption in a pipeline during impact. To this end, a series of indentation experiments carried out on offshore steel pipes covered by a multi-layer polymeric coating solution is performed. The test program includes quasi-static and dynamic denting experiments on both coated and uncoated full-scale pipe cross-sections. All pipes tested have a length of approximately 1 m. The sharpest indenter from the relevant guidelines is used, as a sharp indenter is more likely to penetrate the coating compared with a blunter one. Based on the outcome of the tests, the polymeric coating is found to absorb a considerable amount of the kinetic energy delivered by an impacting object.

1. INTRODUCTION

In the offshore petroleum industry, far-stretching pipeline networks are used to transport crude oil and natural gas along the ocean floor. When specialized protective measures (e.g; trenching, burial, protective covers or armored coatings) either are considered not plausible or too costly [1, 2], pipelines are often left exposed and vulnerable on the seabed. Such pipeline systems are often covered with other coating solutions whose primary

*Corresponding author
Email address: ole.vestrum@ntnu.no (Ole Vestrum)

purpose is not to physically protect, but rather provide corrosion protection, negative buoyancy or thermal insulation. However, while not primarily being designed for it, various coating solutions are known to have beneficial mechanical effects [3–5], such as protection from impacts by foreign objects [6]. As subsea installations tend to attract fish [2], they are sometimes intersected by sharp-edged and massive structures used in fish trawling [2, 7] or struck by falling anchors [3, 8]. Several studies on interaction between bare pipes and foreign objects have been made [9–15]. A general trend in the literature is that while the presence of different coating solutions is observed to influence the pipeline integrity [3, 4, 6], a quantitative evaluation of the isolated contributions are omitted – with a few exceptions [5, 16–18]. As there is a large variation in coating solutions (e.g., material used and design), it is difficult to establish common design rules for all different products. The behavior of only the bare steel has therefore traditionally been used in assessing structural aspects of pipelines. However, in recent issues of the governing pipeline design codes [2, 19], the potential beneficial mechanical effects of coatings are accepted as long as their effectiveness are documented – thus allowing such products to also be included in other aspects of pipeline design, such as impact mitigation. As precipitates form in hydrocarbon fluids when the temperature decreases, pipelines are often insulated with coating products made out of foamed materials. Apart from their excellent thermal properties [20], cellular materials are also known to be great impact mitigators [21]. Due to the progressive damage mechanisms experienced in cellular cores during crushing, combined with the superior rigidity of an internal steel pipe and good ductility of polymers, multi-layer polymeric insulation coatings may be thought to have an especially good mitigating effect during impact events.

As the risk of impact burdens the choice of pipeline design and route, the inclusion of thermal insulation coatings in structural assessments presents a great economical potential. However, there exists little documentation demonstrating the impact mitigating and load distribution effects of polymeric insulating coatings in the published literature. To this end, this work aims to provide experimental results which (i) documents the possible energy absorbing capabilities of a typical polymeric insulating coating system during impact and (ii) investigate the mechanical characteristics of the insulating layer. As a means in achieving these goals, a comprehensive experimental program has been conducted. The response to lateral impact of two different X65 steel pipeline designs, both with and without insulating coating systems, have been studied using quasi-static and dynamic test setups. Coating specimens from one of these coating designs have also been studied in detail both with respect to compressive behavior and structural composition. In addition, quasi-static tensile tests of X65 steel specimens were conducted to ascertain the grade of the internal pipe material. It is believed that the results from this work will provide a proof of concept for polymeric coatings as energy absorbents in design against pipeline impacts, and contribute to the understanding of how such insulation products may be analyzed using simulation tools like the finite element method. However, any simulation attempts are left for further work.

2. IMPACT EVENTS

If a pipeline is left exposed on the seabed, it is vulnerable to impact from foreign objects. de Groot [3] stated that falling and dragging anchors pose a serious threat to subsea equipment. This was exemplified when a 10 ton ship anchor hooked onto and pulled the Kvitebjørn gas pipeline 53 meters out of its installed position [8], which resulted in an extended shut-down period [22]. Another possible interaction is with trawl gear. Bai and Bai [23] distinguished between three occurrences to be considered during trawl gear interference; impact, pull-over and hooking. These events are sometimes mutually exclusive, and differs with respect to loading conditions. During an impact interaction, the loading has a duration less than some hundredths of a second and the response is confined locally to the region of intersection. If the trawl equipment is continuously pulled over the pipeline, large global deformations with significant bending moments and axial forces may be induced. This pull-over action is typically over within a few seconds. The third possible outcome is known as hooking. During this occurrence, the fishing gear does not pass over, but hooks and laterally tows the pipeline out of its initial position. This latter case may cause extreme loads on the subsea installation, but this is a rare event. It is the former of these three interactions, namely impact, which is of immediate interest in the work related to this article. While impact against concrete-coated pipelines have recieved some attention [6, 16, 18], little available research is found in the literature on the impact response of thermally insulated pipes. Because offshore installations in the Norwegian maritime economic zone are required not to an unnecessarily or to an unreasonable degree interfere or hinder fishing activities [2], future occurrences of such events are to be expected. Thus, the pipelines must be designed to sustain impact scenarios.

3. PIPELINE DESIGN

3.1. General

Offshore pipelines are exposed to a range of harsh environmental conditions. Operating on great water depths, large hydrostatic pressures are exerted on the outer surface of the pipeline whilst a multi-phase fluid flow is confined by the inner diameter of the pipe. The fluids hold high temperatures and pressures, which drive the flow through the pipeline. Bare and untreated steel pipes subjected to these environments would suffer greatly under such extreme conditions and heat loss in the oil and gas flow enables the formation of precipitates which could clog the pipe. Therefore, the steel pipes are coated with external layers serving various purposes. Two different polymer-coated pipeline designs illustrated in Figure 1 are studied in this paper. Both designs consist of an inner steel pipe coated with a multi-layer porous polymeric coating system known under the general product name of Thermotite Polypropylene produced by Bredero Shaw (now Shawcor Norway AS) at their facilities in Orkanger, Norway. The complete general coating solution is herein referred to as multi-layer polypropylene (MLPP) and

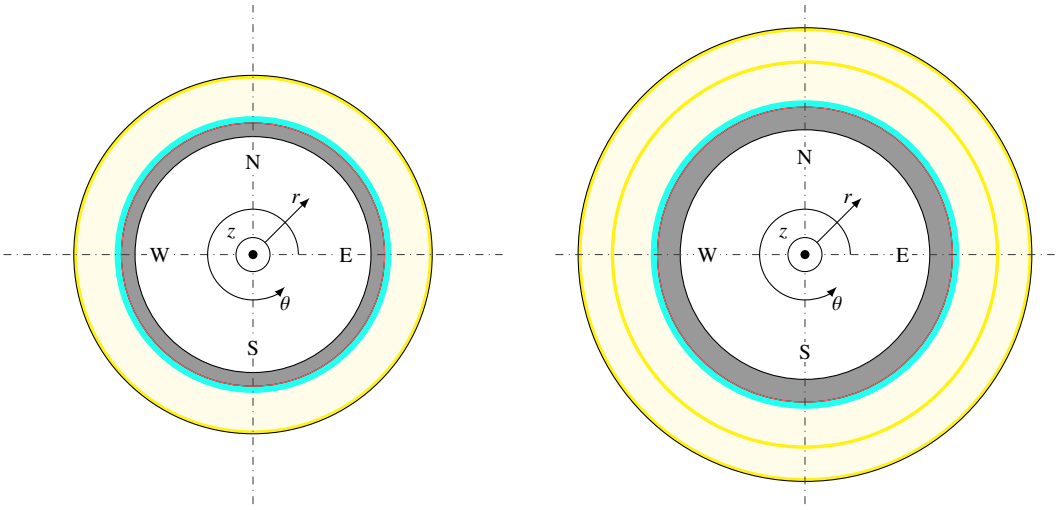

(a) Pipe S. (b) Pipe L.

Figure 1: Cross-sectional view of the two pipeline designs studied herein.

can be produced in a wide range of thicknesses and layer configurations. The innermost portion of the MLPP consists of a three-layer polypropylene coating solution (product name 3LPP) composed of one layer of fusion-bonded epoxy providing corrosion protection, one layer of extruded adhesive and a layer of solid polypropylene. The 3LPP is essentially the same for both designs, though layer thicknesses may differ. The 3LPP is followed by additional insulation layering as a part of the total MLPP solution. The two pipeline designs studied herein are denoted Pipe S and Pipe L and their respective layer configurations are illustrated (in scale) in Figure 1.

Both the geometrical characteristics and the insulation layer compositions vary in the two designs, i.e., the layer thicknesses, diametrical values and total number of layers are different in Pipe S and Pipe L. Figure 2 gives an overview and the values for the different layers in both designs. The values stated in this figure are approximate as they may vary along the pipeline.

3.2. Steel pipeline

The geometries of the inner steel pipe of Pipe S and Pipe L are also different. From Figure 2 it is readily seen that the inner diameter and steel wall thickness of Pipe S are less than that of Pipe L. Both pipe designs are made of X65 grade steel and are produced through the Mannesmann process, which uses the cavity formation along the axial direction in the center of bars subjected to cyclic compression in the radial direction to form thick-walled seamless pipes [24].

3.3. Multi-layer polypropylene coating system

To apply the MLPP, steel pipeline sections are fed through the following three-step process:

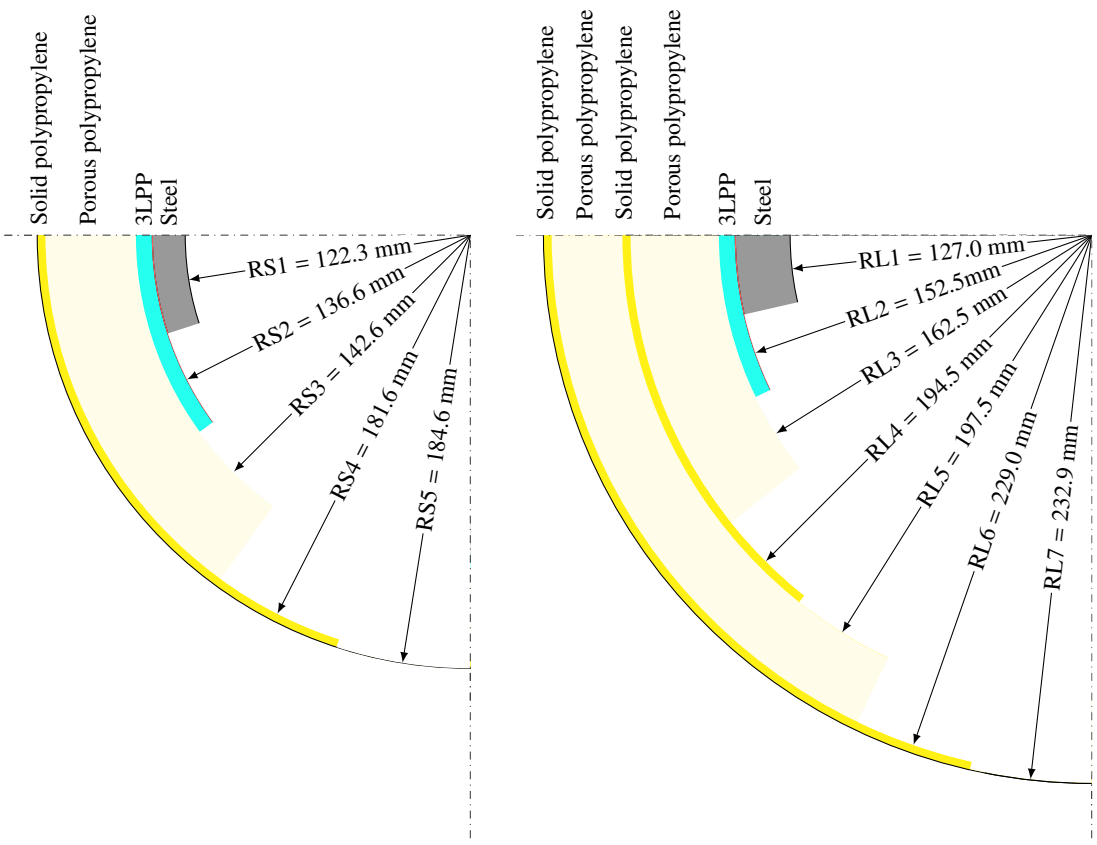

(a) Pipe S.

(b) Pipe L.

Figure 2: Quartile cross-sectional view of layer design for both pipelines studied herein.

1. A preheating and cleaning procedure is performed where corrosion and defects (if detected during visual inspection) are removed through abrasive blasting and surface grinding.
2. An induction heating process heats the pipelines to well above 200°C and the 3LPP solution is applied.
3. The final step applies the thermal insulation system. The process extrudes one thick layer of porous polypropylene and one thin layer of solid polypropylene which act as an outer shield to the ambient seabed environment during operation.

The third step is executed twice for Pipe L, which results in the extra layer-set of porous and outer solid polypropylene compared to Pipe S.

4. PIPE CONSTITUENT CHARACTERIZATION

4.1. Steel pipeline

4.1.1. General

The specification API Spec 5L provides standards for steel pipelines in the natural gas and oil industries [25]. The steel pipelines used in this study are graded X65/L450 according to this specification, which indicates a minimum yield strength of 65 ksi or 450 MPa. The quasi-static stress-versus-strain behavior has been studied for both cross-sectional designs. This was done to check the possible difference in material behavior due to the slightly different deformation history of the steel pipes in both designs. The cross-sectional homogeneity was also checked by retrieving specimens at four different locations along the hoop direction. The locations are marked as N, E, S and W in Figure 1 corresponding to the cardinal points of north, east, south and west along the pipe hoop. These positions are not relative to any obvious reference point since the pipes are seamless and are thus only situated with respect to each other.

4.1.2. Quasi-static uniaxial tension experiments

From samples of both Pipe S and Pipe L, axisymmetric uniaxial tensile test specimens were retrieved across the hoop to check cross-sectional homogeneity and confirm the material grade. All specimens were taken such that their respective axes of symmetry were parallel and oriented along the z-direction as defined in Figure 1. The experiments were performed under quasi-static conditions at an initial strain rate of 10^{-3} s^{-1} over the gauge section of the specimen. A laser micrometer mounted on a mobile frame (described in detail by Fourmeau et al. [26]) continuously recorded the minimum cross-sectional diameters D_r and D_θ, which were the diametrical measures parallel to the cross-sectional r- and θ-directions, respectively, as defined in Figure 1. Through the assumption of negligible elastic strains and plastic incompressibility, the average Cauchy (true) stress, σ, and logarithmic (true) strain, ε, can be inferred through

$$\sigma = F/A \quad \text{and} \quad \varepsilon = \ln\left(A_0/A\right) \tag{1}$$

where F is the force continuously measured by the load cell in the test machine, and A_0 and A are the initial and current minimum cross-sectional area of the specimen's gauge section, respectively. The initial cross-sectional area is calculated as

$$A_0 = \left(\pi/4\right)D_0^2$$

where $D_0 = 3$ mm. The ratio D_r/D_θ was found to be approximately unity throughout the tests, thus giving an indication of isotropic material behaviour, which is consistent with previous work [27]. The current minimum

cross-sectional area was calculated through the relation

$$A = \left(\pi/4\right) D_r D_\theta$$

in post-processing the results.

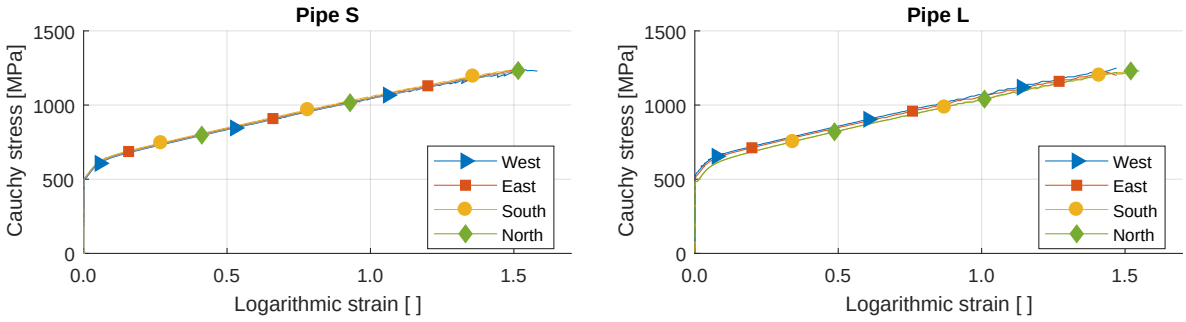

(a) Pipe S.

(b) Pipe L.

Figure 3: Uniaxial tension test results for specimens sampled at four cardinal points along both pipe designs' cross sections. Key parameters are available in Table 1.

Table 1: Initial yield stress (σ_0), ultimate tensile stress (σ_{UTS}), strain at σ_{UTS} (ε_{UTS}), fracture stress (σ_f) and fracture strain (ε_f) retrieved from uniaxial tension experiments for the steel constituent for both Pipe S and Pipe L. The full stress-versus-strain curves are plotted in Figure 3.

(a) Pipe S.

	Point	σ_0 [MPa]	σ_{UTS} [MPa]	ε_{UTS} [ ]	σ_f [MPa]	ε_f [ ]
Pipe S	N / North	487	569	0.125	1252	1.67
	S / South	528	608	0.094	1254	1.69
	E / East	515	598	0.103	1228	1.61
	W / West	482	569	0.121	1254	1.62
	Average	*503*	*586*	*0.111*	*1247*	*1.65*

(b) Pipe L.

	Point	σ_0 [MPa]	σ_{UTS} [MPa]	ε_{UTS} [ ]	σ_f [MPa]	ε_f [ ]
Pipe L	N / North	504	588	0.107	1239	1.63
	S / South	508	597	0.107	1234	1.59
	E / East	493	585	0.110	1247	1.59
	W / West	507	592	0.108	1238	1.65
	Average	*503*	*591*	*0.108*	*1240*	*1.62*

Figure 3 presents the Cauchy stress versus the logarithmic strain from all tests, while Table 1 presents the key results. As the mobile laser continuously measure the minimum diameter in perpendicular directions, the true stress-versus-strain curves in Figure 3 are obtained up to failure. Once a neck develops, a triaxial state of stress is introduced, meaning that the stress measured in Figure 3 is the major principal stress. Both the stress triaxiality and the load path are important for fracture in this material [28]. The pipeline component experiments presented later showed no signs of fracture in the steel, which means that this topic will not be discussed in any detail herein. Figure 3 gives good indications that the material behavior around the cross-section is homogeneous for both Pipe S and Pipe L, and no noticeable difference between the two pipe geometries was observed. The measured yield strength exceeds the minimum requirement indicated through the steel classification, material shows good ductility

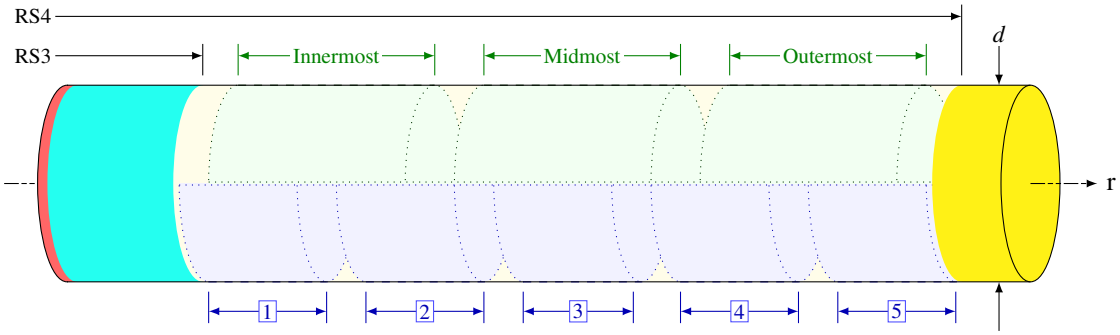

Figure 4: Cylindrical coating column with outlines of two different specimen extraction schemes. The steel part of the cross-section has been omitted in the illustration as this section is dedicated to the multi-layer coating.

with an average failure strain of $\bar{\varepsilon}_f = 1.64$.

Further discussions on fracture and mechanical isotropy in X65 grade steel can be found in previous works [27–29]. This material is also shown to exhibit a moderate degree of strain-rate sensitivity, showing a 20% increase in flow stress for a strain rate of 830 s^{-1} compared with the quasi-static tests [29].

4.2. Multi-layer polypropylene coating system

4.2.1. General

This section presents a limited investigation into the characteristics and mechanical response of coating specimens retrieved from the foamed insulating layer in Pipe S confined by r = RS3 and r = RS4 defined in Figure 2a. The insulating layer makes up over 80% of the design's total coating thickness and is produced in an extrusion process where a propylene copolymer known as BA202E [30] is combined with the foaming agent SAFOAM FP-40 to form the foamed structure. Hegdal et al. [31] studied the variation in thermal conductivity due to changing the pore morphology over the thickness of a similar coating solution. Therein, microtome images where collected from a coating specimen, revealing an anisotropic and inhomogeneous internal pore structure. Efforts have therefore been made to investigate the presence of similar characteristics in the coating used herein through density measurements and X-ray computed tomography. Cellular materials of various densities are used as impact protection in many applications [21] – and this portion of the multi-layer coating system is therefore of particular interest in mitigating pipeline impacts. Hegdal et al. [31] documented significant variation in mass density over the thickness of their coating. As mechanical properties of such materials are often found to be dependent on mass density [21], upsetting tests have been conducted on foamed specimens in order to study possible variations in material behavior throughout the coating layer. In addition, polymeric materials are known to exhibit strain-rate sensitivity, so the coating material's sensitivity to increased strain rates is also investigated.

Cylindrical specimens machined from cylindrical through-thickness coating columns were used for all of the

studies in this section. An example of such a coating column is illustrated in Figure 4 along with specimen geometries related to two different test series.

4.2.2. Morphological variations

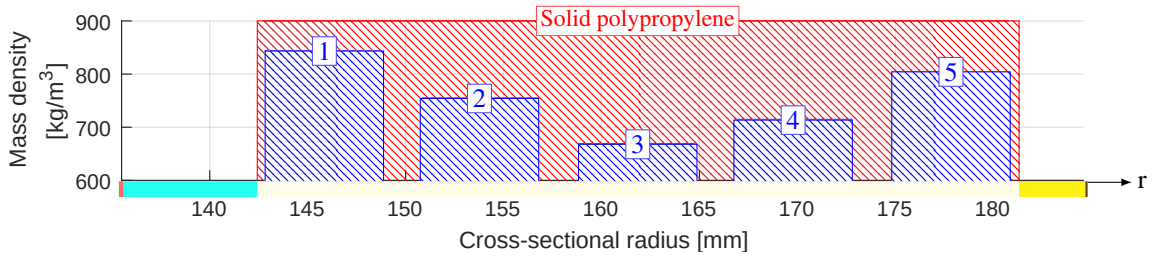

Figure 5: Measured mass density variation between RS3 and RS4 in Pipe S (blue) along with the producer supplied bulk density of polypropylene (red). The numbering of the blue bars are related to the specimens sampled at the positions of the corresponding outlines in Figure 4.

A study on the variation of the mass density along the r-axis (see Figure 1) was performed for Pipe S. Three coating columns were extracted where each column was lathed into five cylindrical specimens. The origins for all of the three columns' specimens are illustrated by the blue outlines in Figure 4, and each region $i \in \{1, 2, 3, 4, 5\}$ along r was measured three times. It was estimated that the machined gap between the specimens was approximately 2 mm. Each specimen had an initial nominal height of $h_0 = 6$ mm and diameter $d_0 = 10$ mm, but they were individually measured using a micrometer and weighed by a 0.02-grams precision scale in order to calculate the corresponding mass density. Figure 5 presents the measured mass density as a function of r at each region i. The deviation in measured density between each region i over the three coating columns was in the magnitude of 1 kg/m^3 so the average of all is presented. A Nikon XT H225 ST MicroCT scanner was then used

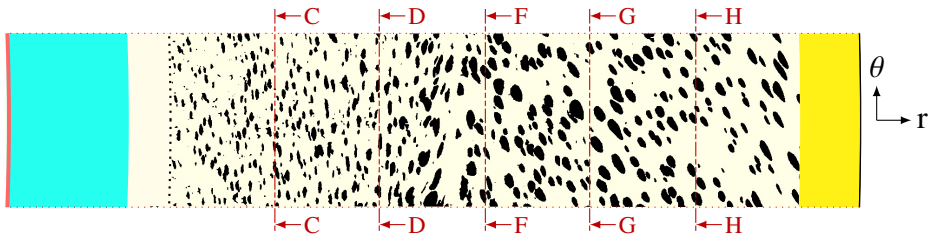

(a) Binarized sectional image slice over a portion of the coating.

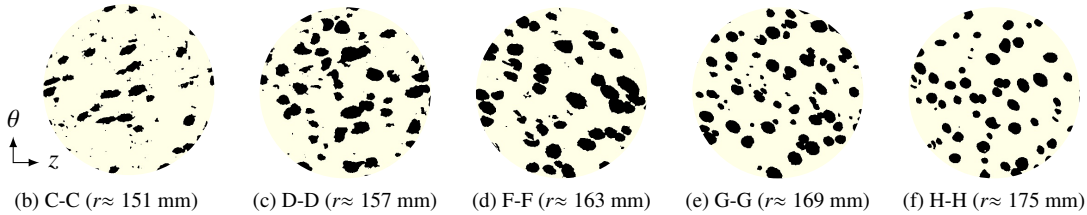

(b) C-C ($r \approx$ 151 mm) (c) D-D ($r \approx$ 157 mm) (d) F-F ($r \approx$ 163 mm) (e) G-G ($r \approx$ 169 mm) (f) H-H ($r \approx$ 175 mm)

Figure 6: Binarized image slices from an X-ray computed tomography scan performed on a cylindrical coating column (see Figure 4) with a diameter of 10 mm. The printed reference system is the same as defined in Figure 1a.

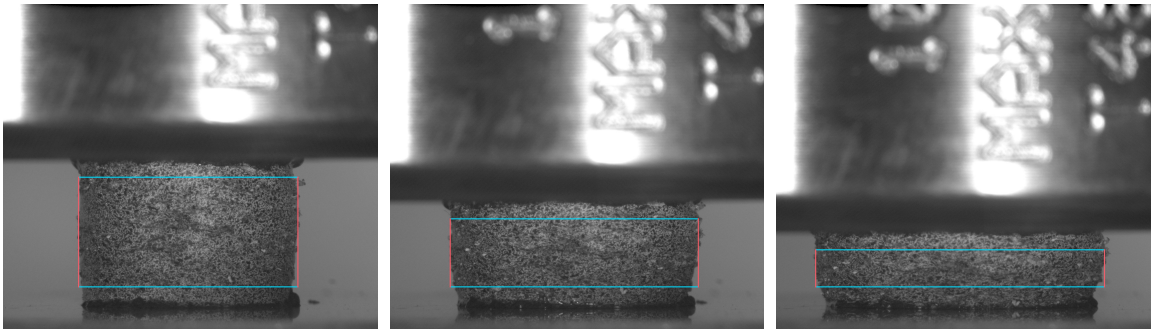

(a) $\varepsilon \approx 0.3$ (b) $\varepsilon \approx 0.6$ (c) $\varepsilon \approx 0.9$

Figure 7: Images from the upsetting test at various strains for a Midmost specimen with outlines of the edge-tracing results. The red lines are the registered peripheral linearized edges of the specimen during compression. See Figure 8a for stress-versus-strain results from this specific test.

to perform an X-Ray Computed Tomography (XRCT) scan on a cylindrical coating column. The scan produced a voxel-resolution of around 20μm $\times$ 20μm $\times$ 20μm and the commercial software Nikon CT Pro 3D (Version XT 3.1.3) was used for volume reconstruction. Figure 6 presents a selection of binary projections from this scan.

By comparing the results presented in Figure 5 and Figure 6, it is seen that regions along r, which seemingly hold the same density profiles, differ notably with respect to pore morphology. The two-dimensional projections of the three-dimensional volume give indications that the pores have ellipsoidal-like shapes within the insulating layer. The foamed layer material appears to be graded meaning that the porous structure varies along one or more of the spatial dimensions of the material. These trends are also consistent with the work done by Hegdal et al. [31].

4.2.3. Mechanical behaviour

Multiple mechanical test series under different loading conditions and with specimens collected across the coating, have been performed. All tests were conducted using an Instron 5982-L2035 test machine [32] with an Instron 2580-301 (100kN) load cell for measuring the forces (F) during compression. In upsetting tests, the inevitable presence of friction will affect the desirable uniaxial stress state. Multi-purpose lubrication was applied to both the top and the bottom of the cylindrical specimens to reduce friction and minimise barrelling effects (which introduce complex states of stress in the specimens). According to the load cell data sheet [33], the force measurements come with an uncertainty of $\pm$ 0.15% at the force levels achieved in the experiments. A 5-megapixel Prosilica GC2450 camera was used to take still images of the deformation process. The load cell and camera output were synchronised to form complete sets of corresponding force and image data at corresponding times. Figure 7 presents three selected images from different points during deformation from one of the upsetting tests. An edge-tracing routine was written to follow the evolution of the peripheral edges of the cylindrical specimen in order to calculate the change in cross-sectional area (A). The results from one such tracking procedure is illustrated by

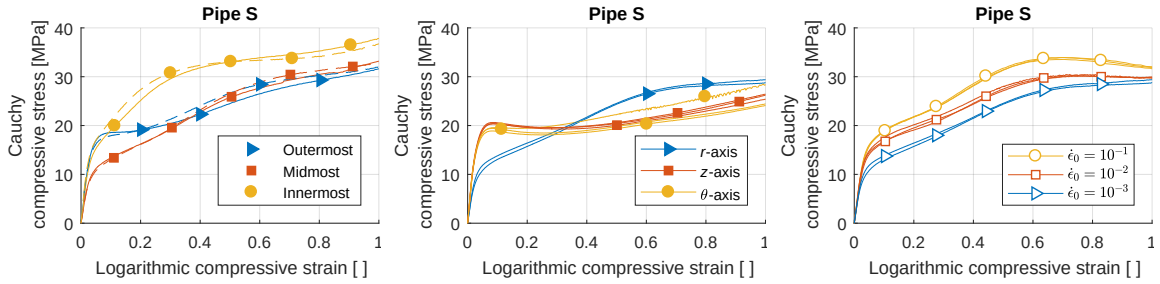

(a) Through-thickness variation. (b) Mechanical anisotropy. (c) Increased strain-rates.

Figure 8: Stress-versus-strain results from the different upsetting test series.

the red lines in Figure 7. All material data from the following tests are presented in the form of Cauchy stress ($\sigma = F/A$) versus logarithmic strain (ε). The displacement logged by the cross-head of the test machine was compared with subset tracking in the image data sets, and the discrepancy was found to be minor at the achieved force levels. Thus, the cross-head displacement was used in the calculation of strains (ε) so that $\varepsilon = \ln(h/h_0)$ where h_0 and h are the initial specimen height and the specimen height throughout the test, respectively. In the following data presentation, the negative signs of the stress-versus-strain have been omitted and replaced with the word compressive' in the figures' axis labels.

Three upsetting studies were performed and the results are presented in Figure 8:

- **Through-thickness variation** (Figure 8a): Two cylindrical through-thickness coating columns were retrieved from which three specimens denoted innermost, midmost and outermost as illustrated by the green outlines in Figure 4 and compressed under quasi-static loading conditions. Both columns had an initial nominal diameter $d_0 = 10$ mm, while the specimens had initial heights $h_0 = 10$ mm (dashed lines in Figure 8a) and $h_0 = 8$ mm (solid lines in Figure 8a).

- **Mechanical anisotropy** (Figure 8b): Cylindrical specimens with axes of symmetry approximately parallel to the three axis (r, z and θ) defined in Figure 1a were extracted and compressed under quasi-static loading conditions. Three repetitions were performed in the z- and θ-direction, while only two repetitions were carried out in the r-direction. The nominal measurements for all specimens were $h_0 = 20$ mm and $d_0 = 20$ mm, and extracted so that their volume center coincided at around $r = 162$ mm.

- **Increased strain-rates** (Figure 8c): The strain-rate sensitivity of specimens collected from the specified coating layers were investigated for three initial strain-rates; $\dot{\varepsilon}_0 = \{10^{-3}, 10^{-2}, 10^{-1}\}$ 1/s. All specimens' respective axes of symmetry were parallel to r and it was strived to have their mass center located in the middle of the foamed layer ($r \approx 162$ mm). The initial nominal geometry for the specimens were $h_0 = 20$ mm and $d_0 = 20$ mm. The r-specimens used in the anisotropy tests are the same as the specimens presented

with the label $\dot{\varepsilon}_0 = 10^{-3}$ 1/s in Figure 8c. Two repetitions were performed at this initial strain-rate, while three repetitions were conducted at the remaining loading rates.

These results will be further discussed in Section 6.

5. PIPELINE COMPONENT EXPERIMENTS

5.1. Preliminary

In the relevant design codes [2, 19], acceptable dents caused by impact are given. Too large indentations could lead to alterations of the inner circular cross-section, stress concentrations or hull collapse – impeding maintenance operations, increasing the risk of fatigue and fracture or complicate further operation. The allowable dent size are given as function of the estimated impact frequency, but can not exceed 5% of the diameter value under any circumstance. Therefore, a comprehensive pipeline component experimental program (inspired by the setup outlined by [2]) was performed to study the behavior of pipelines struck by an indenter. The pipeline indentation response has been investigated under two test conditions:

1. Quasi-static denting of coated and uncoated X65 steel pipes (Section 5.2).
2. Dynamic impact of coated and uncoated X65 steel pipes (Section 5.3).

As impact is a dynamic event, a dynamic test setup will be more realistic. However, a quasi-static test may demand less resources. Efforts have therefore been made to investigate how well a quasi-static test emulates a dynamic test using realistic kinetic energies. Both pipeline designs Pipe S and Pipe L are represented in the program, and the tests for quasi-static denting and dynamic impact are performed in two different experimental rigs. The setups were principally identical in terms of boundary conditions enforced on the specimens, but differed in the manner and rate at which the loads were applied. All pipeline specimens are supported along the entirety of their length, which is approximately 1 m. The uncoated pipeline samples were produced by simply removing the coating system from coated specimens. Figure 9 illustrates the geometry of the indenter used in all tests. The indenter had a nose radius of 10 mm, which is the sharpest nose specified in the relevant guidelines [2]. This design was chosen as a sharper nose tends to perforate the structure more easily [34], thus giving the most conservative results with respect to the guidelines. It is noted that the width of the indenter (300 mm) is less than the outer coating diameter of the smallest pipe design tested (i.e., Pipe S with diameter of 369.2 mm). This means that the indenter will cut into the coating on both edges of the indenter.

A total of 7 quasi-static and 19 dynamic impact tests were performed in the test program. Due to the large number of tests, an identification system has been established to separate them. Each individual test is given a unique tag which consists of a sequence of letters and numbers:

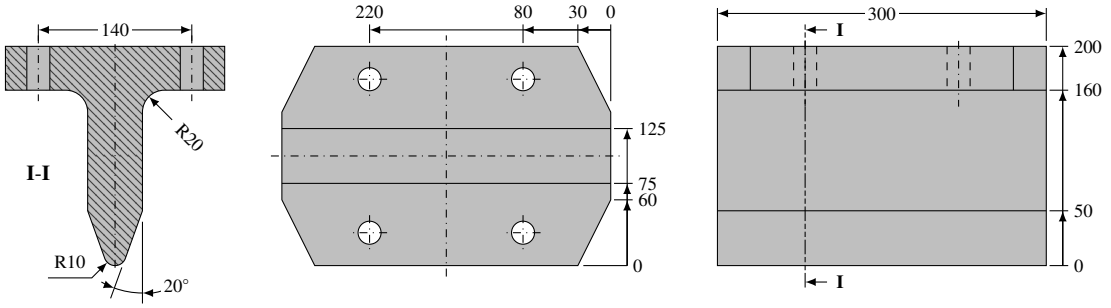

(a) Section I-I. (b) Top view. (c) Front view.

Figure 9: Geometry for indenter used in both quasi-static and dynamic component experiments. Figures (a) and (b) are not to scale. All measures are given in millimetre.

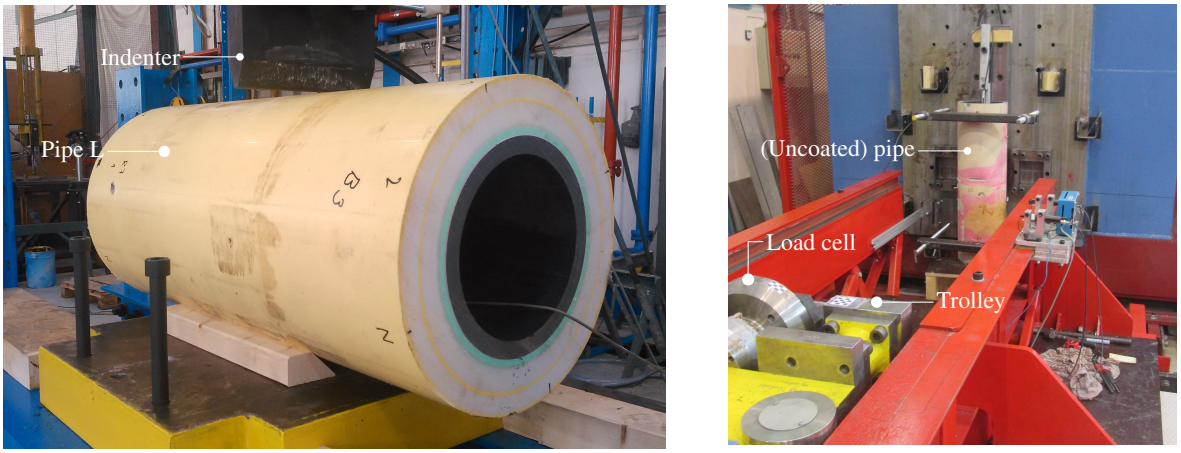

(a) Quasi-static indentation setup. (b) Dynamic impact setup.

Figure 10: Images from the two different test setups used in component experiments.

1. An uppercase Q or D indicates quasi-static or dynamic test conditions, respectively.
2. An uppercase S or L refers to the pipeline design of the sample tested as defined in Figure 1.
3. An integer number which identifies the specific pipeline sample of a given pipeline design.
4. A lowercase letter follows if the respective pipeline sample is used for multiple tests by rotating the specimen.

For the specimens used in multiple tests, the pipes were tested, then rotated 90° and retested. The full experimental program is presented in Table 2 and Table 3. In these tables, selected data from the tests are included as well. Here, w_o and w_i denote the outer and inner deformations, respectively, of the pipelines. The tables also hold a column for F_{peak} which is the maximum force registered by the load cell. Figure 10 shows images from two typical tests – each from the two different experimental setups used in this work.

Table 2: Overview of quasi-static pipeline experiments performed.

ID	Coated	w_o [mm]	w_i [mm]	F_{peak} [kN]
QS1[1)]	No	83	> 52	1052
QS2[1)]	Yes	114	> 52	1355
QL0a[2)]	Yes	94	7	1792
QL0b[2)]	Yes	65	12	2083
QL1	No	44	> 19	2130
QL2a	Yes	102	13	2233
QL2b[3)]	Yes	100	16	2217

1) Inner LVDT reached its limit as seen in Figure 12a.

2) Trial case.

3) QL2a rotated 90° and reused.

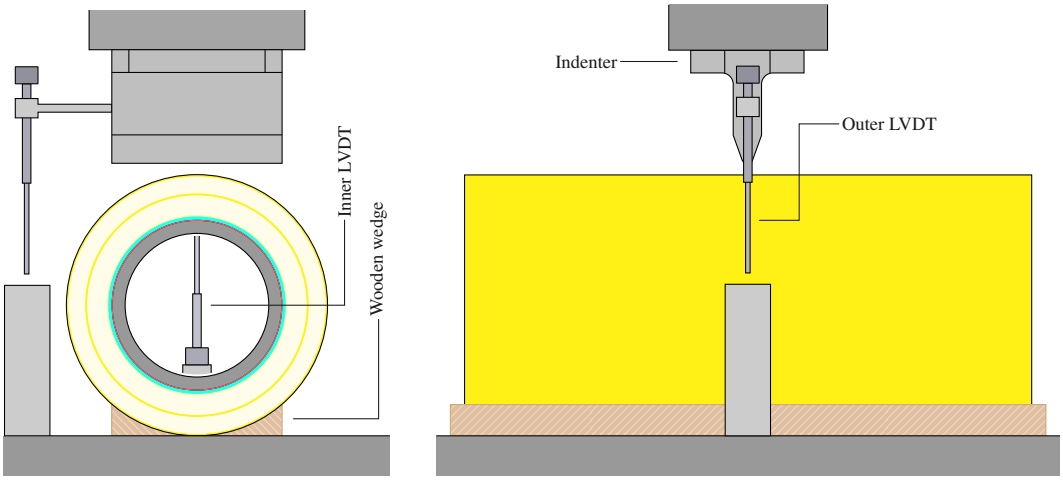

(a) Left side view.

(b) Front view.

Figure 11: Setup for the quasi-static component test.

5.2. Quasi-static pipeline experiments

5.2.1. General

In the quasi-static component tests presented in this section, a deformation controlled hydraulic piston is used. All tests were conducted using an Instron 1800 kN general purpose test machine – with the option of increasing the force to 2300 kN. Table 2 holds an overview of the performed tests in this part of the component test program along with some key features and results.

5.2.2. Setup

Figure 11 illustrates the quasi-static test setup, with a sample of Pipe L as an example. The pipeline sample is placed on a firm steel plate providing rigid support while wooden wedges are placed on either side to prevent the specimen from rolling over. A load cell measures the force while two sets of displacement measures are

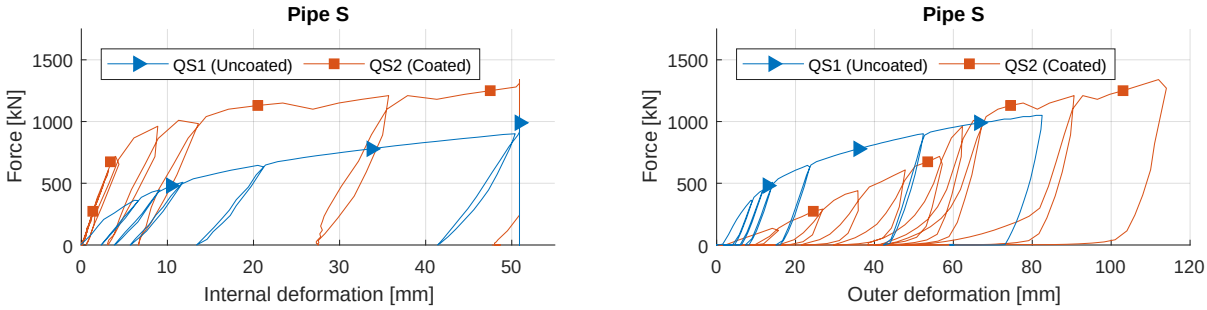

(a) Force versus internal deformation of Pipe S.

(b) Force versus outer deformation of Pipe S.

Figure 12: Results from quasi-static component experiment for Pipe S. The markers in figures (a) and (b) corresponds to the same sampling points in each data set.

logged. Both the internal displacement of the inner steel pipeline wall and the displacement of the indenter are registered using linear variable differential transformers (LVDT). An internal LVDT is mounted directly beneath the contact point between the pipe and indenter, thus measuring the internal deformation of the cross-section. An external LVDT measures the displacement between the indenter and the steel support. These provide more accurate measurements compared with the displacement of the piston which will include any deformation in the testing machine. Some effects of the machine stiffness is expected as the forces achieved during testing are high. Figure 10a shows an image from a specimen of Pipe L in the quasi-static indentation setup.

5.2.3. Execution

Two specimens of pipeline Pipe S were tested – one with and one without the MLPP coating system. These tests are named QS1 and QS2, respectively. Three specimens of Pipe L were tested – one with the MLPP coating system (QL1) and two without (QL0 and QL2). Both coated specimens of Pipe L were tested twice, thus the suffix (a or b) in Table 2 was applied to the tests' identification tag. The experiments related to QL0 were intended as trial cases to control the experimental setup, but are still valid and included in the test matrix. The load was applied with a deformation rate of 10 mm/min in order to achieve quasi-static conditions. At each multiple of 300 kN, the specimen was unloaded and reloaded again. A total of 7 quasi-static tests were performed using this setup.

5.2.4. Results

The first test, QL0a, was loaded with the prescribed 300 kN hysteresis curve to about 1800 kN. This constituted a trial run of the rig and laid grounds for further testing. The next test, QL0b, was carried out on the same pipe as indicated by the number, and the load was increased to maximum without the hysteresis. Due to insufficient lateral support, a beam in the rig suffered lateral torsional buckling and had to be replaced. Additional stiffeners were added, and testing could resume. A higher peak load was attained in the following tests compared with

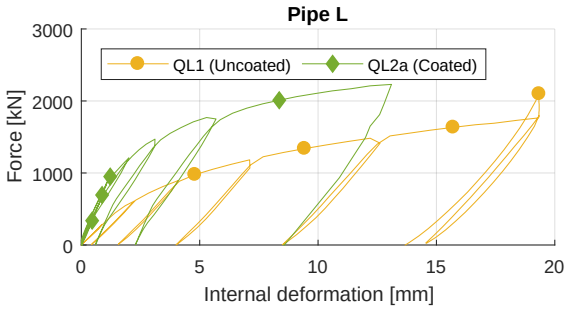

(a) Force versus internal deformation of pipe L.

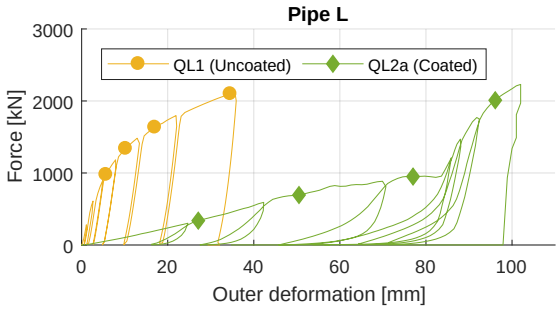

(b) Force versus outer deformation of pipe L.

Figure 13: Results from quasi-static component experiment for Pipe L. The markers in figures (a) and (b) corresponds to the same sampling points.

previous tests (see Table 2). Force versus displacement results for pipe QL0 are omitted for brevity as they were very similar to QL2.

Force versus displacement curves from quasi-static testing of Pipe S are plotted in Figure 12 with Figure 12a using the inner deformation and Figure 12b using the outer deformation as measured by the LVDTs. As expected, the coated pipe suffers larger outer deformation for an equivalent force as the coating is more compliant than the steel material while the internal deformation is significantly less. The results from test QS2 in Figure 12b indicates a fairly linear behavior for deformation up until about the magnitude of the coating thickness. Up until the second hysteresis loop in QS2 (force levels at about 600 kN), there are no permanent internal deformation of the coated steel as seen in Figure 12a. When the coating is penetrated and the indenter reaches the steel, the force increases markedly. Some dips in the curve for QS2 are registered – which may be a consequence of the various layers of coating rupturing successively. This means that the coating contributes significantly in reducing the deformation of the inner steel pipe, and a much higher force is needed to attain the same level of internal deformation than without the coating. The internal deformation was only measured up to about 51 mm in the experiments with Pipe S, as the LVDT had to be removed in order to avoid damaging it.

The corresponding force versus displacement results in the component tests for Pipe L are presented in Figure 13, and the results indicate the same mitigation contribution of the coating system as for those of Pipe S. Again, the coated pipe behaves quite linearly until the steel is engaged, at which point the slope of the force versus outer deformation (Figure 13b) increases significantly. This effect is even more pronounced in the tests related to Pipe L due to the thicker external coating, and both larger diameter and thickness of the inner steel pipeline. For QL2a, the three first load steps (300 kN, 600 kN and 900 kN) yield no or minor plastic inner deformations of the pipe. Note that the inner LVDT suffered an error during testing of the QL1, as seen at the end of the associated graph in Figure 13a.

Table 3: Overview of dynamic pipeline experiments performed.

ID	Coated	v_0 [m/s]	E_{kin} [kJ]	w_o [mm]	w_i [mm]	F_{peak} [kN]
DS1[1)]	No	6.33	29.5	47	> 35	850
DS2a	Yes	5.10	19.1	50	0.0	661
DS2b	Yes	6.31	29.3	62	5.5	939
DS3a	Yes	5.21	20.0	52	0.0	641
DS3b	Yes	6.33	29.5	62	4.3	969
DS4a	Yes	3.70	10.1	37	0.0	484
DS4b	Yes	7.32	39.4	72	11.8	1045
DL1	No	6.29	29.1	23	11.8	1801
DL2a	Yes	5.14	19.4	47	0.0	692
DL2b	Yes	6.26	28.8	59	0.0	764
DL3a	Yes	5.21	20.0	49	0.0	733
DL3b	Yes	6.26	28.8	59	0.0	748
DL4a	Yes	3.77	10.5	36	0.0	490
DL4b	Yes	7.30	39.2	72	0.0	794
DL5a[2)]	Yes	3.76	10.4	34	0.0	486
DL5b	Yes	7.30	39.2	73	0.0	788

1) Out of range for laser.

2) Corrupt laser output data.

5.3. Dynamic pipeline experiments

5.3.1. General

As a pipe impact is a dynamic event, the program also includes pipeline experiments with rapid loading. Trawling equipment may reach velocities of about 3.0 m/s [2], and the size and shape of potential impacting objects can vary significantly. In 2014, the trawling gears in use could weigh up to 9 tonnes [2]. These conditions equates to a kinetic energy of 40.5 kJ. The kinetic energies used in the tests are comparable to the calculated kinetic energies based on the actual mass and velocities used under practical fish trawling. However, the addition of the water mass to the total mass of the impacting object, has not been accounted for in these experiments. While higher kinetic energies may be achieved by increasing the velocity of the impacting object, it is understood that a too large deviation from realistic impact velocities in tests may trigger incomparable responses.

5.3.2. Setup

As previously stated, it is reasoned that the setup for the dynamic impact pipeline experiments is chiefly the same as the corresponding quasi-static setup, albeit a different rig was used. Rather than applying a deformation via a displacement controlled hydraulic jack, a trolley with a mass of 1472 kg (and equipped with a load cell) is accelerated to a prescribed velocity to deliver a given amount of kinetic energy to the pipe specimen. To this end, a pendulum accelerator [35] was used to launch the trolley. Figure 14 illustrates the conceptual setup for the dynamic component tests. Now, the specimens are mounted vertically as opposed to the quasi-static setup.

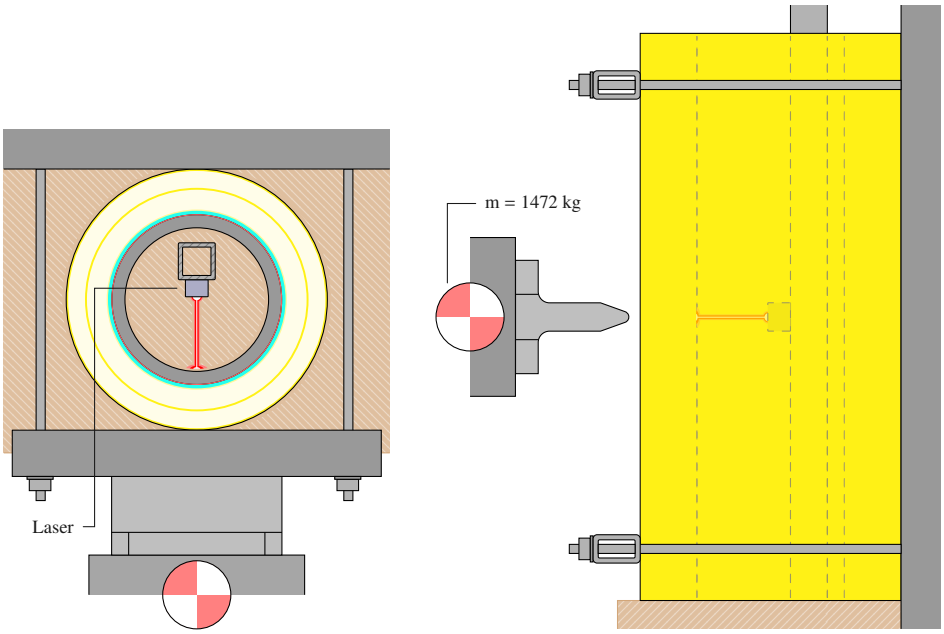

(a) Bottom view. (b) Left side view.

Figure 14: Setup for dynamic impact test.

Clamps were used to secure the pipeline specimens at desired locations. The very same indenter (see Figure 9) as in the quasi-static tests was used. Due to the limited sampling rate of the LVDT, an optoNCDT 2300-100 laser displacement sensor [36] (referred to as laser in this text) was used to measure the internal deformation of the steel pipe. The outer deformation was inferred from the load cell measurements and time integration [35] and signal drift was corrected for using imaging techniques [37]. The laser was mounted on a beam going through the entire length of the pipe, and the beam was secured to the reaction wall as illustrated in Figure 14. The position of the laser was adjusted to align with the position of the indenter thus measuring the maximum internal deformation of the cross-section as in the quasi-static tests. A Phantom v1610 high-speed camera recording at 15000 frames per seconds was used to capture the events. Figure 10b shows an image from the dynamic experimental setup after a finished test on an uncoated specimen. The trolley with the attached indenter and load cell is seen in the foreground of the image while the mounted pipeline sample held in place by clamps can be seen in the background.

5.3.3. Execution

Both coated and uncoated pipe specimens of Pipe S and Pipe L were included in this part of the experimental program. A wide range of impact energies (10 to 40 kJ) were tested governed by controlling the initial velocity of the trolley. The rig performed well in producing the desired initial velocities for the trolley. With the exception of the uncoated pipes, all pipes were impacted twice. The lower impact energy was always used first when testing a pipe twice, as this would cause the least permanent deformation of the steel in the pipe (if any). The pipes were

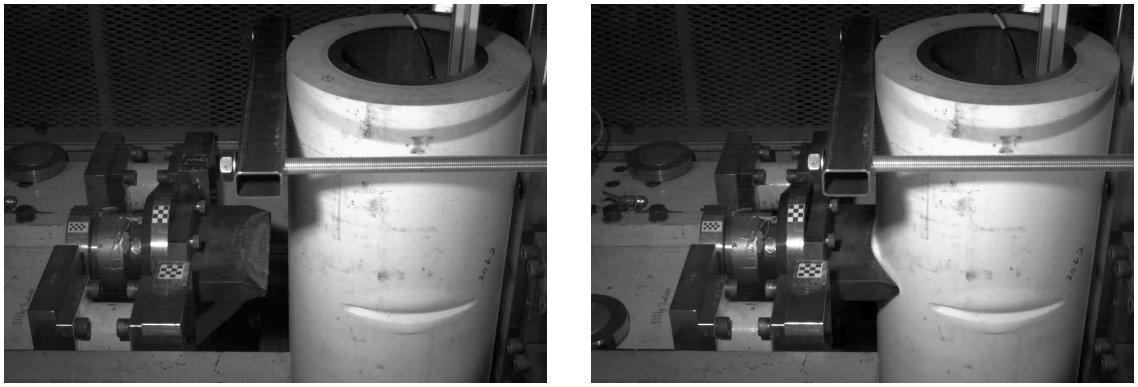

(a) Before indenter impact.

(b) After indenter impact.

Figure 15: Two images taken with the high-speed camera during test DL3b where $v_0 = 6.26$ m/s. Note the permanent indentation in the coating caused by test DL3a in the frontward facing part of the pipe sample.

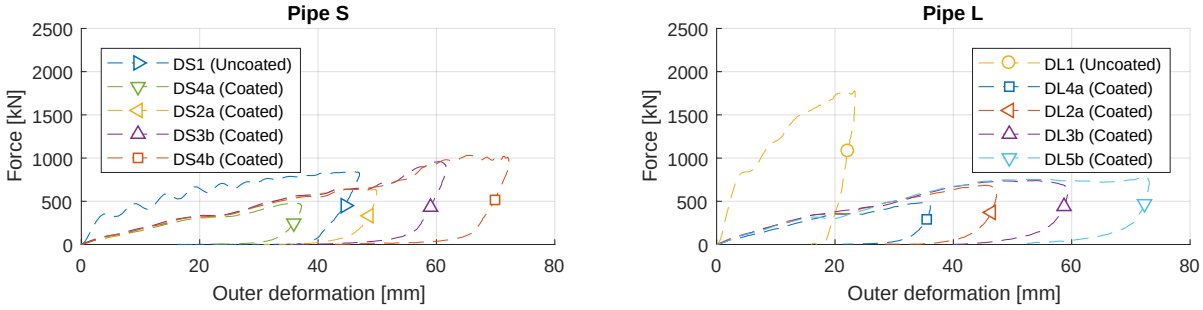

(a) Pipe S.

(b) Pipe L.

Figure 16: Results from the dynamic component experiments for Pipe S and Pipe L over a variety of impact energies.

then rotated 90° and tested again. There was no evidence to suggest that the first impact exerted any significant influence on the second as the observed damage was found to be very localized in the tests. Key results from the dynamic program are presented in Table 3. Figure 15 presents two images taken from the high-speed recordings from DL3b before (Figure 15a) and during (Figure 15b) impact. The local deformation from test DL3a is seen from the images.

5.3.4. Results

Table 3 lists key test parameters and results; the initial velocity v_0 for the trolley and the adhering kinetic energy E_{kin}, the outer maximum deformation w_o obtained from the load cell and the maximum inner deformation w_i as measured by the laser, and the peak force F_{peak} measured by the load cell. Again, the results were both consistent and reproducible with low scatter. Figure 16a and Figure 16b show the force-versus-outer deformation curves for the specimens of Pipe S and Pipe L, respectively. It is foremost observed that the uncoated specimens of both designs were a lot stiffer initially and retained higher force levels throughout the entire deformation than

their coated counterparts. This is especially prominent for the Pipe L specimens. It is also seen from Table 3 that only impact energies above 20 kJ caused any permanent internal deformation of the coated Pipe S specimens. Only elastic deformations in the order of a few millimeters were registered for the lower impact energies. For the impact energies in the range of 30 kJ to 40 kJ, plastic deformation was recorded, but this was at most 2% and 5% of the cross-section's inner diameter, respectively. Equivalently, an impact energy of 30 kJ caused an inner deformation of about 14-15% for the uncoated specimen of Pipe S. For the tests performed on coated specimens of Pipe L, no plastic deformations were registered within the investigated impact energy range of 10 kJ to 40 kJ. However, some inner elastic deformations were registered. The force-versus-outer displacement curves for the sampled impact energies show a very consistent response. The uncoated specimen of Pipe L, it reached a final deformation of 11.8 mm (4% of the inner diameter) at an impact energy of 30 kJ.

5.4. Test setup efficiency

The guideline [2] that describes a similar test setup as used herein, puts forth some requirements to the experimental rig. Therein, it is stated that the mass and stiffness of the support should be ten times larger than the accelerated mass and stiffness of the initial shell design of the pipeline specimen. The test rig used in the dynamic impact tests had a reaction wall of 150 tonnes and was made of solid steel and concrete. The supports were thus deemed sufficient. Table 3 supplies the kinetic energies in the performed dynamic impact tests based on the initial velocity v_0 and the mass of the trolley in the test setup. By performing a numerical integration of the force-versus-outer displacement, an estimate of the work done on the impacting mass may be calculated. The work done on the indenter up until the point of maximum deformation should be equivalent to the calculated initial kinetic energy based on the initial velocity and mass measurements. Out of all valid dynamic impact tests (n=16) the average ratio between the work done on the impactor and the initial kinetic energy was 97.8% with a standard deviation of 0.2%. The trapezoidal integration technique, force, mass and velocity measurements and drift in the time integration may be possible sources of error. The latter source of error was checked through comparisons with the high-speed camera images. It was seen that the procedure of numerical integration of the force-versus-outer displacement curves yields reasonable results.

6. Discussion

Two test setups were used to examine the response of both coated and uncoated pipelines at component level. In terms of boundary conditions, the setups were assumed to be equivalent, while the rates at which the loading was applied differed between the two. For the dynamic impact test configuration, a range of impact energies was examined (from 10 to 40 kJ), which produced good repeatability for both pipe designs as presented in Figure 16. It is reasoned that within the examined impact energy range, no significant change in deformation modes occurs

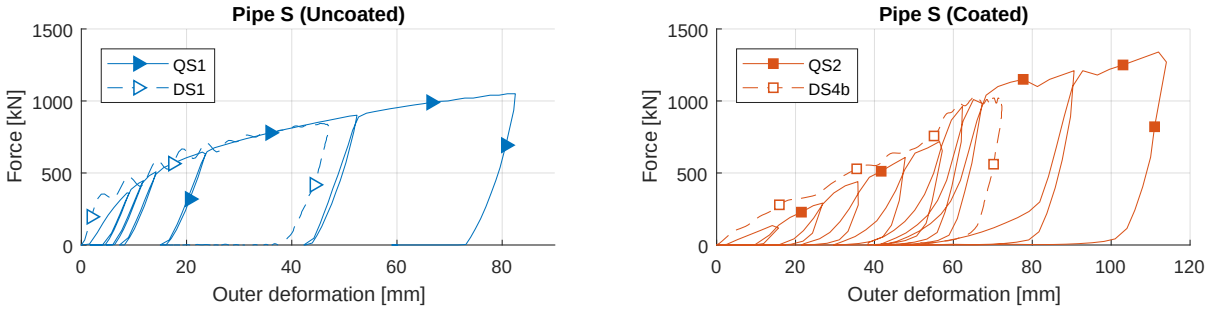

(a) Uncoated specimens of design Pipe S.

(b) Coated specimens of design Pipe S.

Figure 17: Comparison of the quasi-static and dynamic indentation test results for Pipe S.

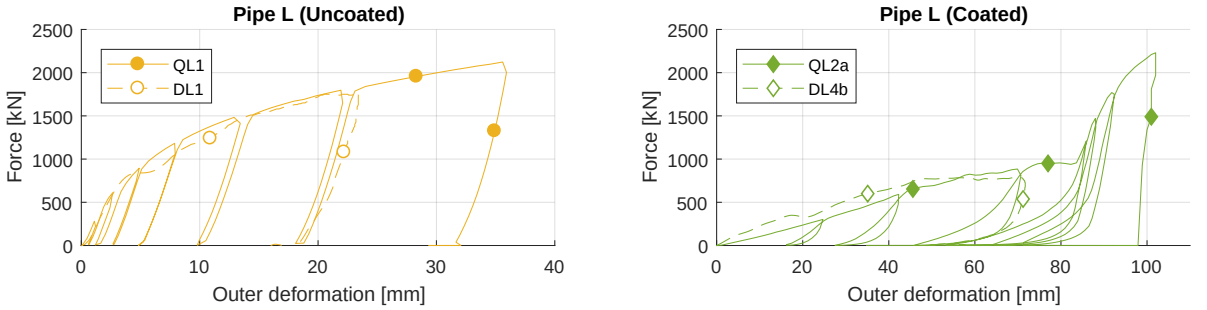

(a) Uncoated specimens of design Pipe L.

(b) Coated specimens of design Pipe L.

Figure 18: Comparison of the quasi-static and dynamic indentation test results for Pipe L.

as no major difference in the dynamic loading histories are seen over the initial velocity spectrum. However, this is not necessarily correct when assessing the total deformation response of longer pipeline sections. An actual impact on an operational pipeline would likely cause both local deformations (confined to the area of intersection) and global deflection (due to stretching and bending) of a larger portion of the pipeline. Alsos et al. [38] and Igland et al. [39] investigated the importance of velocity and mass on the response for uncoated pipelines when impacted by objects with equal kinetic energies. Their studies involved larger pipeline sections where also global deformations were triggered as a cause of the impacts. They found that increasing impact velocity in order to achieve a desired kinetic energy (as done herein) will increase the local denting in a full pipeline. This is because inertia effects will inhibit global deflection when the loading is applied rapidly – thus the energy is dissipated locally instead. It is therefore reasonable to assume that the indentation levels reached herein are conservative due to the absence of global deflection in the experiments. External coating might also have a further beneficial effect during global deformations due to increased energy dissipation from axial straining in the full pipeline, but this is outside the scope of this paper.

Only one single indenter geometry was used in the presented studies. It is reasoned that the shape of the

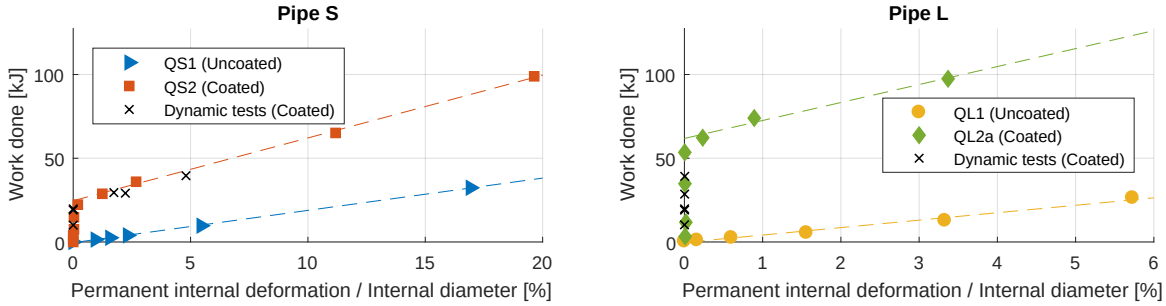

(a) Pipe S.

(b) Pipe L.

Figure 19: Work done on the indenter versus the ratio between the permanent internal deformation and the initial diameter of the inner steel pipe.

impacting object may play an important role in the indentation behaviour as it influences how the loading is distributed in the pipeline during impact. The indenter chosen for this study represent the worst case from the guidelines [2]. During the experiments, some shearing of the coating by the indenter was observed. A wider and more blunt indenter would likely distribute the load in a way which compresses larger portions of the coating. By engaging more coating, more energy would be dissipated through increased surface friction and plastic deformation. The angle at which the indenter strikes the pipeline is also important in this respect – an oblique incident angle could be argued to further increase friction and coating activation. Thus, the relatively sharp edge of the indenter and perpendicular incident angle used herein are therefore argued to provide conservative results.

Larger deformations were achieved in the quasi-static tests compared to the dynamic tests. Figure 17 and Figure 18 reveal comparable force-versus-outer displacement curves in the investigated kinetic energy range. From these plots, it is reasoned that a quasi-static test setup may be used as a viable test configuration when mapping the local indentation behavior during dynamic impact loading of these coated pipeline designs – at least within the velocity range considered here.

By integrating the force-versus-outer displacement curve from a quasi-static test to a given energy value, a reasonable estimate of the corresponding indentation caused by an impact event can be obtained. The quasi-static tests were conducted using sequences of loading/unloading at each multiple of 300 kN, which produced corresponding values of permanent outer and inner deformation. Design codes and guidelines traditionally use the permanent outer deformation of the steel pipeline in limit state designs. The allowable dent size in the internal steel pipe's outer diameter after impact varies based on operating conditions, but the absolute maximum value is set to 5% of the pipe's initial outer diameter under any set of conditions. However, the outer deformation of the inner steel pipe covered by the multi-layer coating was not logged in this study. Instead, the internal deformation values are used in the following reasoning. In Figure 19, the maximum work done on the indenter (up until that stage) from quasi-static tests on both uncoated and coated samples of Pipe S (Figure 19a) and of Pipe L (Figure 19b)

is plotted against the ratio between the internal deformation at the end of each unloading stage and the initial diameter of the respective inner steel pipe. The work is estimated by numerically integrating the force-versus-outer deformation curves from the corresponding tests. The work done is compared with the kinetic energies from the dynamic tests of coated pipes presented in Table 3. Two points are to be made from Figure 19a and Figure 19b.

1. A large amount of energy is absorbed in the coating before any significant deformation is seen of the pipeline's innermost hoop for both designs.
2. A slight increase in the slopes during deformations of coated tests compared to the uncoated analogues is found. This indicates that the polymeric coating continues to contribute to energy absorption even after the deformation of the steel pipe has initiated.

At internal deformations values below 0.07% (as seen in Figure 19), Pipe S reaches work values of around 25 kJ while Pipe L gets up to about 60 kJ of work. It is reasoned that the majority of the deformation of the cross-section is confined to the coating layers up until this stage. The indenter is, however, seen to exert no significant work on the uncoated specimens before permanent internal deformation starts to accumulate in both designs.

Apart from the previously mentioned considerations (indenter design and incident angle, increased impact velocity and lack of global deflection), other aspects like pipeline support and pressurization will influence the conservatism of the results. The steel/concrete foundation used herein, which supports the specimens, should be more rigid than other realistic seabed conditions (like sand, clay or gravel). Palmer et al. [18] concluded that a sand foundation reduced the indentation by one-third when compared to a steel support. In addition, a pressurized hull is also experienced to better withstand indentation compared to an unpressurized one [40, 41]. The chosen foundation and absence of internal pressure are therefore argued to add to the conservatism of the results.

A consistent and significant variation over the foamed layer is seen in the through-thickness study in Figure 8a. For instance, the midmost region exhibits a substantially lower initial yield stress, while at $\varepsilon \approx 0.3$ and above, the stress-versus-strain response for the midmost and outermost regions seem to coincide. However, the stress levels for the innermost specimens are significantly higher than the other two. If assuming that the intrinsic material behavior of the solid constituent remains isotropic and constant throughout the thickness of the layer, the pores are seen to have a pronounced influence on the mechanical behavior, and therefore the energy absorption during deformation. Due to the rigidity of the steel hoop, deformations are localized in the more compliant coating layers. This localization of deformation spares the critical steel pipe – until the coating is sufficiently compressed. Dense solids are relatively incompressible when compared to porous analogues, which experience significant volume change during deformation [21]. As cellular materials are compressed, the cells will collapse and eventually become packed at a limiting strain level. This limiting strain is known as the densification strain and is closely linked to the density of the cellular material [21]. As a porous material densifies, an increase in stiffness will

occur. A lower density is typically associated with a greater densification strain, but at a lower stress level. This stress behavior is seen in Figure 8a were the midmost (and least dense) specimen has the lowest stress response, at least initially. As the stress-versus-strain integral is related to the amount of dissipated energy, the optimum density value (with respect to impact mitigation) is therefore not trivial. Gibson and Ashby [21] defines materials with densities less than 30% of its constituent material as cellular. Figure 5 presents a density variation from around 70 to 100% of dense polypropylene, which places the insulation material in an intermediate material class between cellular and dense. While low-density foams are known to exhibit minor lateral straining when subjected to uniaxial deformation, a clear increase in specimen diameter is seen in Figure 7. Foams are also known to deform under nearly constant stress (when compressed) between initial yield and densification, but only the stress-versus-strain response of the specimens with axes of symmetry parallel to z- and θ-directions (see Figure 8b) are observed to exhibit a similar response. What causes this discrepancy remains to be understood. A consistent increase in stress is seen even at slightly elevated strain-rates in Figure 8c. Whether this is due to intrinsic behavior of the polypropylene or the foamed internal structure, is not known, but such a material feature may be of importance for a pipeline's response to impact events.

The material studies conducted herein are limited and there might be several other factors that complicate the mechanical characterization of polymeric porous coatings. Coating products as the one used herein are known as wet insulation where the material will experience water absorption dependent on ambient pressure, fluid media and temperature history [42, 43]. Water uptake and temperature will inevitably alter the immediate polymer's material behaviour [44], but the presence of high water content and elevated temperature exposure may also have long-term consequences for the mechanical response as polymeric coatings are known to degrade over time, i.e., ageing [43, 45]. Polymer foams are also known to be prone to material creep which may alter the morphology of the coating during operation [46]. However, such aspects are outside the scope of this paper, and require future studies.

7. Concluding remarks

The goals of this work were to provide experimental results that that (i) documented the possible impact mitigating capabilities of insulation coating systems and (ii) to investigate mechanical characteristics of the coatings. The main conclusions from these studies are:

(i) The experimental work conducted herein proves that polymeric insulating solutions may indeed absorb considerable amounts of energy during impact. In fact, the smallest tested cross-section (with the thinnest coating) dissipated the full kinetic energy of the most extreme impact situation outlined in relevant guidelines while sustaining less than 5% permanent deformation of the internal hull diameter. In order for the uncoated pipe to halt an equivalent moving object, the internal diameter had to undergo close to 20% permanent deformation. For Pipe L, a coated steel pipeline would suffer no significant permanent deformation under even the most extreme impact situations. The coatings are also seen to provide an increase in energy dissipation even after the steel pipe has been engaged – for both pipeline designs.

(ii) The coating of Pipe S was observed to have significant variations in its porous morphology and compressive stress-versus-strain across the thickness. It is reasoned that much of the variation in the mechanical response may be related to the corresponding pore structure, although the possibility of slight property gradients in constituent polypropylene are not to be excluded. This cellular variation may influence how and how much energy are absorbed during impact. By relating a given cellular structure to a mechanical response, the mitigating effect under other load conditions and with other coating designs could possibly be estimated. X-ray computed tomography presents itself as a viable tool in acquiring such detailed information of thermal coatings' pore structure.

As full-scale component tests are both difficult and expensive to perform, future work should be focused on developing numerical approaches for estimating the impact mitigating contribution from thermal insulation. Finite element method (FEM) based assessments are becoming common practice in design processes. The lack of material models which adequately describes a porous material's behavior inhibits use of such advanced computational tools. Apart from the obvious considerable impact mitigating effect documented through the pipeline component tests, the material studies of the coating revealed a rather complex material behavior – which is not easily reproduced with FEM. Polymeric coatings which continuously varies from very porous to fully dense will definitely require advanced modeling approaches to accurately capture global behaviors, e.g., the total energy absorption due to deformation of a complete multi-layer solution. In addition to varying material properties within a given coating product, there exists a large variety of different solutions from different manufactures. This calls for a generic assessment approach which a FEM framework may offer. A properly developed and calibrated finite element model could be used to optimize pipeline designs not only towards sustaining impact from objects, but also with respect to other loading scenarios and thermal insulation. Further efforts should therefore be made towards the material modeling of porous polymer materials used in multi-layer coating systems to adequately incorporate them into modern simulation frameworks – and eventually be used with design guidelines.

8. ACKNOWLEDGEMENTS

The present work has been carried out with the financial support from Centre for Advanced Structural Analysis (CASA) through the Research Council of Norway's Centre for Research based Innovation (CRI) scheme (project 237885). Thankful acknowledgements are made to Dr. Ing. Erik Levold at Equinor (formerly Statoil) for his contributions and for supplying the test specimens.

9. REFERENCES

[1] R.J. Brown. OTC 1570 Pipelines can be designed to resist impact from dragging anchors and fishing boards. *Offshore Technology conference*, 1972. doi: https://doi.org/10.4043/1570-MS.

[2] DNV GL. DNVGL-RP-F111 Interference between trawl gear and pipelines. May 2017. Recommended practice.

[3] S.J. de Groot. The impact of laying and maintenance of offshore pipelines on the marine environment and the north sea fisheries. *Ocean Management*, 8(1):1 – 27, 1982. ISSN 0302-184X. doi: https://doi.org/10.1016/0302-184X(82)90011-7.

[4] R.T. Igland and T. Søreide. OMAE2008-57354 Advanced pipeline trawl gear impact design. *International Conference on Offshore Mechanics and Arctic Engineering*, 3: Pipeline and Riser Technology; Ocean Space Utilization:271–277, 2008. ISSN 978-0-7918-4820-3. doi: https://doi.org/10.1115/OMAE2008-57354.

[5] G. R. Howell and Y. F. Cheng. Characterization of high performance composite coating for the northern pipeline application. *Progress in Organic Coatings*, 60(2):148 – 152, 2007. ISSN 0300-9440. doi: https://doi.org/10.1016/j.porgcoat.2007.07.013.

[6] H. Moshagen and S.P. Kjeldsen. OTC 3782 Fishing gear loads and effects on submarine pipelines. *Offshore Technology Conference*, 1980. doi: https://doi.org/10.4043/3782-MS.

[7] The Petroleum Safety Authority Norway. Rørledningsskader - Skader og hendelser fra Petroleumstilsynets CODAM database. `http://www.psa.no/getfile.php/1345620/PDF/Roerledningsskader%200ktober2017.pdf`, 2017. [Online; accessed 7-December-2017].

[8] E. Gjertveit, J.O. Berge, and B.O. Søvik. OTC 20814 The Kvitebjørn Pipeline Repair. *Offshore Technology Conference*, 2010. doi: https://doi.org/10.4043/20814-MS.

[9] C.G. Soares, A.M. ASCE, and T.H. Søreide. Plastic analysis of laterally loaded circular tubes. *Journal of Structural Engineering*, 109(2), 1983. doi: https://doi.org/10.1061/(ASCE)0733-9445(1983)109:2(451).

[10] N. Jones, S.E Birch, R. S. Birch, L. Zhu, and M. Brown. An experimental study on the lateral impact of fully clamped mild steel pipes. *Proceedings of the Institution of Mechanical Engineers, Part E: Journal of Process Mechanical Engineering*, 206(2):111–127, 1992. doi: https://doi.org/10.1243/PIME_PROC_1992_206_207_02.

[11] W.Q. Shen and K.S. Chen. An investigation on the impact performance of pipelines. *International Journal of Crashworthiness*, 3(2):191–210, 1998. doi: https://doi.org/10.1533/cras.1998.0070.

[12] A. Manes, R. Porcaro, H. Ilstad, E. Levold, M. Langseth, and T. Børvik. The behaviour of an offshore steel pipeline material subjected to bending and stretching. *Ships and Offshore Structures*, 7(4):371–387, 2012. doi: https://doi.org/10.1080/17445302.2011.606699.

[13] M. Kristoffersen, F. Casadei, T. Børvik, M. Langseth, and O.S. Hopperstad. Impact against empty and water-filled X65 steel pipes - Experiments and simulations. *International Journal of Impact Engineering*, 71 (Supplement C):73 – 88, 2014. ISSN 0734-743X. doi: https://doi.org/10.1016/j.ijimpeng.2014.04.004.

[14] V. Longva, S. Sævik, E. Levold, and H. Ilstad. Dynamic simulation of subsea pipeline and trawl board pull-over interaction. *Marine Structures*, 34(Supplement C):156 – 184, 2013. ISSN 0951-8339. doi: https://doi.org/10.1016/j.marstruc.2013.09.004.

[15] J.X. Yu, Y.Y. Zhao, T.Y. Li, and Y. Yu. A three-dimensional numerical method to study pipeline deformations due to transverse impacts from dropped anchors. *Thin-Walled Structures*, 103(Supplement C):22 – 32, 2016. ISSN 0263-8231. doi: https://doi.org/10.1016/j.tws.2016.02.006.

[16] R. Wang, L.H. Han, and Z. Tao. Behavior of FRP-concrete-steel double skin tubular members under lateral impact: Experimental study. *Thin-Walled Structures*, 95(Supplement C):363 – 373, 2015. ISSN 0263-8231. doi: https://doi.org/10.1016/j.tws.2015.06.022.

[17] M.A. Polanco-Loria, H. Ilstad, and E. Levold. A numerical-experimental approach of indentation problem: Part ii – force-dent response of polymeric coated steel pipes. *International Conference on Offshore Mechanics and Arctic Engineering*, Volume 5B: Pipelines, Risers, and Subsea Systems, 2017. doi: 10.1115/OMAE2017-61902.

[18] A. Palmer, M. Touhey, S. Holder, M. Anderson, and S. Booth. Full-scale impact tests on pipelines. *International Journal of Impact Engineering*, 2006.

[19] DNV. DNV-OS-F101 Submarine Pipeline Systems. October 2013. Offshore Standard.

[20] G.P. Guidetti, G.L. Rigosi, and R. Marzola. The use of polypropylene in pipeline coatings. *Progress in Organic Coatings*, 27(1):79 – 85, 1996. ISSN 0300-9440. doi: https://doi.org/10.1016/0300-9440(95)00523-4. Proceedings of the 20th International Conference in Organic Coatings Science and Technology.

[21] L.J. Gibson and M.F. Ashby. *Cellular Solids: Structure and Properties*. Cambridge Solid State Science Series. Cambridge University Press, 2 edition, 1997. doi: https://doi.org/10.1017/CBO9781139878326.

[22] J. Sheehan. Kvitebjorn pipe leak. `https://sysla.no/international/kvitebjorn_pipe_leak/`, 2008. [Online; accessed 7-December-2017].

[23] Y. Bai and Q. Bai. Chapter 12 - trawl impact, pullover and hooking loads. In *Subsea Pipelines and Risers*, pages 173 – 194. Elsevier Science Ltd, 2005. doi: https://doi.org/10.1016/B978-008044566-3.50014-2.

[24] A. Ghiotti, S. Fanini, S. Bruschi, and P.F. Bariani. Modelling of the mannesmann effect. *CIRP Annals - Manufacturing Technology*, 58(1):255 – 258, 2009. ISSN 0007-8506. doi: https://doi.org/10.1016/j.cirp.2009.03.099.

[25] PM International Suppliers. API 5L X Grades: X52 X56 X60 X65 X70 Welded & Seamless Pipe API 5LX. `http://www.api5lx.com/api5lx-grades/`, 2017. [Online; accessed September-2017].

[26] M. Fourmeau, T. Børvik, A. Benallal, and O.S. Hopperstad. Anisotropic failure modes of high-strength aluminium alloy under various stress states. *International Journal of Plasticity*, 48(Supplement C):34 – 53, 2013. ISSN 0749-6419. doi: https://doi.org/10.1016/j.ijplas.2013.02.004.

[27] M. Kristoffersen, T. Børvik, I. Westermann, M. Langseth, and O.S. Hopperstad. Impact against X65 steel pipes - An experimental investigation. *International Journal of Solids and Structures*, 50(20):3430 – 3445, 2013. ISSN 0020-7683. doi: https://doi.org/10.1016/j.ijsolstr.2013.06.013.

[28] M. Kristoffersen, T. Børvik, and O.S. Hopperstad. Using unit cell simulations to investigate fracture due to compression-tension loading. *Engineering Fracture Mechanics*, 162(Supplement C):269 – 289, 2016. ISSN 0013-7944. doi: https://doi.org/10.1016/j.engfracmech.2016.04.044.

[29] M. Kristoffersen, T. Børvik, M. Langseth, and O.S. Hopperstad. Dynamic versus quasi-static loading of X65 offshore steel pipes. *The European Physical Journal Special Topics*, 225(2):325–334, 2016. doi: https://doi.org/10.1140/epjst/e2016-02629-4.

[30] Borealis. BA202E, Polypropylene Block Copolymer for Non-Pressure Pipes. `http://www.borealisgroup.com/en/polyolefins/products/Others/ba202e/`, 2017. [Online; accessed September-2017].

[31] J.P. Hegdal, T.R. Tofteberg, T. Schjelderup, E.L. Hinrichsen, F. Grytten, and A. Echtermeyer. Thermal conductivity of anisotropic, inhomogeneous high-density foam calculated from three-dimensional reconstruction of microtome images. *Journal of Applied Polymer Science*, 130(2):1020 – 1028, 2013. ISSN 1097-4628. doi: https://doi.org/10.1002/app.39238.

[32] Instron. 5980 Floor Model Systems for High-Capacity Universal Testing. `http://www.instron.us/en-us/products/testing-systems/universal-testing-systems/electromechanical/5900/5980-floor-model`, 2017. [Online; accessed January-2017].

[33] Instron. 2580 Series static load cells. `http://www.instron.us//~/media/literature-library/products/2016/09/2580-series-load-cells.pdf?la=en`, 2016. [Online; accessed January-2017].

[34] A. Palmer, A. Neilson, and S. Sivadasan. Pipe perforation by medium-velocity impact. *International Journal of Impact Engineering*, 32(7):1145 – 1157, 2006. ISSN 0734-743X. doi: https://doi.org/10.1016/j.ijimpeng.2004.09.010.

[35] A.G. Hanssen, T. Auestad, T. Tryland, and M. Langseth. The kicking machine: A device for impact testing of structural components. *International Journal of Crashworthiness*, 8(4):385–392, 2003. doi: https://doi.org/10.1533/ijcr.2003.0246.

[36] Micro-epsilon. optoNCDT Laser displacement sensors. `https://www.micro-epsilon.com/download/products/_laser-sensor/dax--optoNCDT-2300--en-us.html`, 2017. [Online; accessed May-2018].

[37] E. Fagerholt. eCorr Digital Image Correlation. `https://www.ntnu.edu/kt/ecorr`, 2017. [Online; accessed May-2018].

[38] H.S. Alsos, R.T. Igland, and T.H. Søreide. Evaluation of pipeline impact damage. *International Conference on Offshore Mechanics and Arctic Engineering*, 2012.

[39] R.T. Igland, H.S. Alsos, and S.O. Kvarme. Advanced pipeline impact design. *International Conference on Offshore Mechanics and Arctic Engineering*, 2016.

[40] N. Jones and R.S. Birch. Impact behaviour of pressurised pipelines. *Structures Under Shock and Impact X*, pages 219–228, 2008.

[41] M. Kristoffersen, M. Langseth, and T. Børvik. Combined three-point bending and axial tension of pressurised and unpressurised offshore steel pipes – experiments and simulations. *Submitted for possible journal publication*, 2018.

[42] D. Choqueuse, A. Chomard, and C. Bucherie. OTC 14115 Insulation materials for ultra deep sea flow assurance : Evaluation of the material properties. *Offshore Technology Conference*, 2002.

[43] V. Sauvant-Moynot, N. Gimenez, and H. Sautereau. Hydrolytic ageing of syntactic foams for thermal insulation in deep water: degradation mechanisms and water uptake model. *Journal of Materials Science*, 2006.

[44] B.J. Turner. NACE-11030 Polypropylene Coatings for High Temperatures and Thermal Insulation of Pipelines. *NACE CORROSION 2011 Conference & expo*, 2011.

[45] N. Guermazi, N. Haddar, K. Elleuch, and H.F. Ayedi. On the peel behavior of polymer coating-steel system: Effect of hygrothermal aging. *Advances in Polymer Technology*, 2010. doi: https://doi.org/10.1002/adv.20188.

[46] A.M. Harte, D. Williams, and F. Grealish. A coupled temperature-displacement model for predicting the long-term performance of offshore pipeline insulation systems. *Journal of Materials Processing Technology*, 2004.